This is the Pre-Published Version.
The following publication Deng, E., Yang, W., He, X., Zhu, Z., Wang, H., Wang, Y., ... & Zhou, L. (2021). Aerodynamic response of high-speed trains under crosswind in a bridge-tunnel section with or without a wind barrier. Journal of Wind Engineering and Industrial Aerodynamics, 210, 104502 is available at https://doi.org/10.1016/j.jweia.2020.104502.

Aerodynamic response of high-speed trains under crosswind at bridge-tunnel section with or without wind barrier

Weichao Yang [a, b)], E Deng [a, *)], Xuhui He [a, b)], Zhihui Zhu [a, b)], Ang Wang [a)], Zhao Wen [a)]

a): School of Civil Engineering, Central South University, Changsha 410075, China.

b): National Engineering Laboratory for High Speed Railway Construction, Changsha 410075, Hunan, China

*): Corresponding author.

E-mail address: weic_yang@csu.edu.cn (W.C. Yang); denge12@csu.edu.cn (E Deng); xuhuihe@csu.edu.cn (X.H. He); zzhh0703@163.com (Z.H. Zhu); 315037875@qq.com (A. Wang); 2607431990@qq.com (W. Zhao)

Abstract: The high-speed train is suddenly impacted by crosswind when it travels to the bridge–tunnel section, thereby seriously affecting its safety. In this study, a 3D computational fluid dynamics (CFD) numerical model of train–tunnel–bridge–wind barrier is established on the basis of delayed detached eddy simulation (DDES) turbulence model and porous media theory, and a dynamic analysis model of wind–train–bridge coupling is combined. The influences of wind barrier with height of 3 m and porosity of 30% on aerodynamic coefficient, flow field structure and running safety of high-speed train under crosswind in the bridge–tunnel section are studied. Results indicate that, the abrupt effect of the aerodynamic coefficients is significantly weakened by more than 50% with wind barrier. The aerodynamic fluctuation amplitudes in the bridge–tunnel section are 1.25–5.5 times higher than those in the bridge section. The difference of the pressure distribution in the longitudinal direction is significantly reduced, because of the obstruction and diversion of the wind barrier and the space limitation on the windward side. Accordingly, the abrupt amplitude of the aerodynamic coefficients in the bridge–tunnel section is reduced, so is the safety of train running. The bridge–tunnel section is the weak link of safety control. Adopting the wind barrier with the same parameters for the bridge–tunnel section as the bridge section is obviously unreasonable and should be separately designed.

Keywords: bridge-tunnel section; wind barrier; high-speed train; aerodynamic response; flow field structure; running safety

1. Introduction

With the rapid development of high-speed railway in mountainous areas, the connecting section of bridge and tunnel has been commonly used in high-speed railways. The proportion of bridge and tunnel in the Guizhou section of the Shanghai–Kunming high-speed railway, China, has reached 81%. The special valley topography is prone to generate strong crosswind. The aerodynamic performance of high-speed trains (HSTs) intensively changes, and the running safety is reduced when the trains pass through the bridge and tunnel connecting section under strong crosswind (Deng et al., 2020a, 2020b; Yang et al., 2018; Wei et al., 2018; Li et al., 2015). Wind barrier is usually used as the windproof measure on the bridge to ensure the safety of HST and stability of bridge (Guo.et al., 2015a; Zhang et al., 2013).

Many scholars have conducted lots of studies on the influences of wind barrier on the aerodynamic performance and running safety of HSTs on the bridge in recent years. Avila-Sanchez et al. (2016) analyzed the flow field distribution above a railway bridge equipped with solid windbreaks through wind tunnel tests. Olmos et al. (2018a) evaluated the influence of wind barriers and tuned mass dampers in the train's running safety. Guo et al.(2015a) investigated the aerodynamic effects of wind barriers on the HST-bridge system. The results have showed that the side force and rolling moment coefficients of HST efficiently reduce with wind barrier, whereas they increase in the bridge deck. He et al. (2016, 2014) studied the influences of wind barrier height and porosity on the aerodynamic characteristics of the train at the bridge. The results have indicate that the wind barrier's parameters should be optimized. Kozmar et al. (2014) explored the effects of porosity and height of wind barrier and the orientation of barrier elements on flow and turbulence using particle imaging technology. The optimal wind barrier parameters are 30% porosity and 5 m height. Zou et al. (2018) evaluated the aerodynamic characteristics of an alighting bridge wind system with or without wind barriers. Wind barriers could improve the surface pressure distribution of high-speed trains on the bridge, thereby improving the aerodynamic performance. Xiang et al. (2014) measured the wind load of a train through wind tunnel test and calculated the dynamic response of a vehicle using a coupled vibration method of windmill and bridge system. Thus, the protective effect of wind barrier was determined.

The above-mentioned studies mainly focus on HSTs running in the bridge wind barrier area completely and ignore the transformation of trains running in different infrastructures. Yang et al. (2019, 2018) and Deng et al. (2019a) found that transient variations of the flow field structure and aerodynamic characteristics occur when trains move into the tunnel under crosswind, thereby reducing running safety. Liu et al. (2017) found that the pressure, force, and moment coefficients clearly and suddenly increase when the trains pass through the windbreak transition region under crosswind. Therefore, the wind barrier effect is extremely important to ensure running safety when HSTs pass through the bridge and tunnel connecting section under the transverse wind.

Zhang et al. (2013) used a wind–train–bridge model to study the effects of wind barriers on the dynamic response of trains and proposed the critical train speeds with respect to different wind velocities. Olmos et al.(2018b) evaluated the train running safety over a high-pier viaduct from the Spanish railway network. Montenegro et al. (2019) evaluated the train running safety over two bridges using the normative wind model. Li et al. (2005) presented an analytical model for the dynamics of wind–train–bridge systems in the time domain with wind, where rail vehicles and bridge are modeled as a coupled vibration system. Guo et al. (2015b) and Xia et al. (2008) established a dynamic model of wind–train–bridge system and considered 27 degrees-of-freedom (DOFs) in the vehicle system. The wind excitations on the train and the bridges were numerically simulated using the static tricomponent coefficients obtained from wind tunnel test. The wind–vehicle–bridge coupling analysis system is relatively well developed, but the external load obtained from the wind tunnel test is static or quasi-static. Deng et al. (2019a) obtained the time-history data of train's aerodynamic load through computational fluid dynamics (CFD) calculation and inputted into the 31-DOFs vehicle–track coupling system to realize the corresponding change in aerodynamic load in accordance with the different positions of the train. In this study, the transient aerodynamic loads of the train and bridge were obtained through CFD calculation. Then, they are imported into the wind-train–bridge coupled dynamic system for the analysis of running safety.

In this study, a 3D CFD numerical model of train–tunnel–bridge–wind barrier is proposed to calculate the transient aerodynamic load of the train and bridge on the basis of delayed detached eddy simulation turbulence model and porous media theory. The transient aerodynamic load is inputted into the wind–train–bridge coupling dynamic system to realize the dynamic analysis of running safety. The influence and mechanism of wind barrier on the aerodynamic sudden change performance of HSTs in the tunnel–bridge (out of the tunnel 'OUT' and into the tunnel 'IN') and bridge sections ('BR') are studied from the perspective of train aerodynamic coefficient, flow field structure, and pressure coefficient. The effects of wind barrier on running safety are discussed on the basis of the variation characteristics of train derailment coefficient (DC) and wheel load reduction rate (WLRR).

2. CFD model

2.1. Turbulence model

In this study, the highest running speed of CRH3 is approximately 350 km/h, and its Mach number is close to 0.3. Air is regarded as a compressible fluid. The Reynolds number (Re) of the fluid near the HST is more than 2×10^6, which is in turbulent state. At present, the simulation of turbulent flow mainly includes Reynolds-Averaged Navier–Stokes simulation (RANS), detached eddy simulation (DES), and large eddy simulation (LES). RANS (Zou et al., 2018; Li et al., 2019; Lu et al., 2020) treats the vortices of different scales equally in the flow field, smoothens the details of the temporal and spatial variations of pulsation motion through average operation, and has poor prediction for large separation flow when the turbulence model is established. LES can well simulate large separation flow. However, LES is unsuitable to be widely used in engineering because the mesh is extremely dense in the boundary layer and the simulation of a large number of small-scale pulsation motion calculation is huge with the current computer level. DES is a method combining RANS and LES that can completely utilize the advantage of the small calculation amount of the Reynolds average method in the boundary layer and simulate the large-scale separated vortex in the area far from the surface of object (Niu et al., 2018).

Delayed DES (DDES) based on the two equations of SST *k–ω* is used in this study to simulate the unsteady compressible transient flow field. The turbulence model is widely used in simulating the flow field structure of HST's movements (Niu et al., 2018). The use of *k–ω* turbulence model near the wall can better simulate the transport of the adverse pressure gradient boundary layer, and the use of *k–ε* turbulence model far from the wall can better simulate the fully developed turbulent flow. According to Wang et al. (2018), the control equations of SST k–ω are expressed as follows:

$$\frac{\partial \rho k}{\partial t}+u_i\frac{\partial \rho k}{\partial x_i}=\frac{\partial}{\partial x_j}\left[\Gamma_k\frac{\partial k}{\partial x_j}\right]+G_k-Y_k \tag{1}$$

$$\frac{\partial \rho \omega}{\partial t}+u_i\frac{\partial \rho k\omega}{\partial x_i}=\frac{\partial}{\partial x_j}\left[\Gamma_\omega\frac{\partial \omega}{\partial x_j}\right]+G_\omega-Y_\omega+D_\omega \tag{2}$$

where ρ is the air density (ρ=1.225 kg/m^3); k is the turbulent kinetic energy; ω is the dissipation rate of turbulent kinetic energy; u_i is the velocity component, subscripts i, j= x, y, z; G_ω denotes the term of turbulent kinetic energy generation caused by velocity gradient; Γ_k and Γ_ω denote the convection terms for k and ω, respectively; Y_k and Y_ω denote the effective diffusion terms of k and ω caused by turbulence, respectively; D_ω denotes the cross convection term, and the propagation of turbulent shear stress is considered by turbulent viscosity.

The coefficient of eddy viscosity v_t is expressed as follows:

$$v_t=\frac{a_1 k}{\max(a_1\omega;\ \Omega F_2)} \tag{3}$$

$$F_2=\tanh(\arg_2^2), \arg_2=\max\left(2\frac{\sqrt{k}}{0.09\omega y};\frac{500\nu}{y^2\omega}\right) \tag{4}$$

where Ω is the absolute value of vorticity; F_2 is the blending function, and a_1=0.31 is the empirical coefficient.

The transition from the *k–ω* model near the wall to the *k–ε* model far from the wall is controlled by mixed function F_1, as shown in Eq. (5).

$$F_1 = \tanh(\arg_1^4)$$
$$\arg_1 = \min\left(\max\left(\frac{\sqrt{k}}{0.09\omega y};\frac{500\nu}{y^2\omega}\right);\frac{4\rho\sigma_{\omega 2}k}{CD_{k\omega}y^2}\right) \tag{5}$$
$$CD_{k\omega} = \max\left(2\rho\sigma_{\omega 2}\frac{1}{\omega}\frac{\partial k}{\partial x_j}\frac{\partial \omega}{\partial x_j};10^{-20}\right)$$

where y is the distance to the next surface; ν_t is the eddy viscosity and $CD_{k\omega}$ is the positive portion of the cross-diffusion term. Model coefficients $\sigma_{\omega 2}$=0.856.

2.2. Porous media model

The porous media model adds a source term representing the momentum consumption in the momentum equation (Eq. (2)). The source term includes viscous loss and inertial loss terms (Maruyama, 2008). The two important parameters, viscous and inertial resistances, are determined to be 2.111×10^8 and 105.28, respectively. The equation is expressed as follows:

$$S_i = -\left(\sum_{j=1}^{3} D_{ij}uv_j + \sum_{j=1}^{3} C_{ij}\frac{1}{2}\rho|v|v_j\right) \tag{6}$$

where S_i is the source term of the momentum equation (i=x, y, z); $|v|$ is the absolute value of the velocity; D_{ij} represents the seepage coefficient; and C_{ij} represents the pressure loss coefficient.

For isotropic porous media, coefficient matrices D and C are simplified into a diagonal matrix, where the diagonal elements are α and C_2, and the other elements are 0. Eq. (6) can be rewritten as follows:

$$S_i = -\left(\frac{u}{\alpha}v_i + C_2\frac{1}{2}\rho|v|v_i\right) \tag{7}$$

where α is the permeability coefficient.

The permeability term (the first term in Eq. (7)) can be ignored, and only the inertial resistance term (the second term in Eq. (7)) in the incoming flow can be considered when the porous media is in high-speed flow. In this study, the coefficient C_2 is deduced in accordance with the empirical formula:

$$C_2 = \frac{1}{C^2}\frac{\left(A_p/A_f\right)^2 - 1}{t} \tag{8}$$

where A_f is the total area of the hole; A_p is the total area of the porous media; C is the coefficient related to Re and t/D (D is the hole diameter and t is the plate thickness), and the coefficient is approximately 0.98 when t/D>1.6, Re>4000.

2.3. Geometric model

The train geometry model is Chinese CRH3 HSTs. It adopts three carriages (head, middle, and tail carriage) to simulate the actual motion of the train (Deng et al., 2020a, 2019a; Niu et al., 2018). The geometric model is built in accordance with the full size (scale ratio is 1:1). The length, height, and width of the train are 76.125, 3.89, and 3.2 m, respectively. Pantograph, windows, and bogie are ignored, as shown in Fig. 1. The distance from the bottom of the train to the bridge is 0.2m. The train is initially located on a flat ground, the distance from the head train to the tunnel entrance is 80 m, and an open area of 43.875m behind the train.

The bridge and tunnel connecting section is composed of two tunnels connected by bridge: tunnel (200 m)–bridge (159 m)–tunnel (200 m), as shown in Figs. 3(a) and 4. The geometric model of the bridge is the 32 m simple-supported box girder commonly used in Chinese high-speed railway, where the pier, track, and other ancillary structures are ignored. The tunnel adopts the standard double-line tunnel section, with the inner contour area of 100 m^2, and the corresponding obstruction ratio is 0.149. The wind barrier adopts a porous medium model and is set along the two sides of the bridge. The wind barrier parameters are 0.1 m thickness, 3 m height, and 30% porosity, as shown in Fig. 2.

2.4. Grid model

The numerical model uniformly adopts a structured grid that is divided into three regions, namely, dynamic grid, static grid and porous media regions, as shown in Fig. 3(c). The train's motion is realized through the technique of layering (Yang et al., 2019, 2018) and sliding grids (Niu et al., 2017b; Liu et al.,2017), and the region around the train is set as dynamic grid region. The porosity of wind barrier is realized by adjusting the coefficient of the porous media model, and this area is the porous media area. The remaining regions are all static grid regions. The grid size of the body surface is approximately 0.1 m and evenly expands outward, as shown in Fig. 3(b). Grid encryption processing near the surface of HSTs, bridges, and wind barriers is set to 10 layers to fully consider the boundary layer effect. The thickness of the first boundary layer is $h_0=1\times10^{-3}$ m, the corresponding value of $y+$ is close to 10 (Paz et a., 2017), and the total thickness of boundary layer is 8×10^{-2} m. The total number of model grids is approximately 32 million, and the integral mesh is shown in Fig. 3(a).

2.5. Boundary conditions and solution settings

The ground and wall surface of tunnel and bridge are set as nonslip wall boundary (wall). The train surface is set as moving wall. The boundary condition of the open space on the bridge is set as pressure far-field, and the Mach number is used to adjust the wind speed. Overlapping surfaces are found between the dynamic grid and static grid regions and between the porous media and static grid regions, as shown in Fig. 3(b), which are set as the interface boundary. The interface can transfer data energy. In the process of calculation, the boundaries at both ends of the dynamic zone always remain stationary. The pressure outlet boundary is used in the initial open space of the train movement and tunnel outlet, as shown in Fig. 4. The purpose of setting the initial open area is to make the flow field structure reach a stable state when the train enters the bridge and tunnel section and simulate the real crosswind environment.

The discrete mode of the governing equation is the finite volume method (FVM). A pressure-based transient compressible solver is used in this simulation. SIMILE algorithm is used to solve the coupling equation of pressure and velocity. Time adopts an implicit equation with second-order precision, and the physical time step of present calculation is determined to be 1×10^{-4} s (Niu et al., 2018). The number of iterations for each time step is 50 or the minimum convergence value of each time step is less than 10^{-6} (Deng et al, 2019; Niu et al., 2017a).

2.6. HSTs aerodynamic load

The resistance of HSTs mainly causes energy consumption and slightly affects train safety. This study mainly investigates the variation characteristics of lateral force (F_z), lift force (F_y), rolling moment (M_x), yawing moment (M_y), and pitching moment (M_z), as shown in Fig. 5.

The carriage surface is divided into several sections when calculating the aerodynamic load. The time history data of mean pressure for each section are extracted through CFD. Thus, the calculation formula of HSTs aerodynamic load is obtained, the detailed formula can be found in reference of Yang et al. (2020).

2.7. Bridge aerodynamic load

The lateral force (F_{bz}), lift force (F_{by}), and rolling moment (M_{bx}) of the bridge are studied, as shown in Fig. 5. The influence of the wind barrier should be considered when calculating the aerodynamic load of the bridge. The wind barrier is taken as part of the bridge and treated in sections. The calculation formula of aerodynamic load of the bridge can be obtained as follows:

$$\begin{aligned} F_{bz} &= \sum_{i=1}^{m}\left(\sum_{j=1}^{l}\left(p_{i,j}\cdot S_{i,j}\cdot\left(\boldsymbol{m}_{i,j}\cdot\boldsymbol{z}\right)\right)\right) \\ F_{by} &= \sum_{i=1}^{m}\left(\sum_{j=1}^{l}\left(p_{i,j}\cdot S_{i,j}\cdot\left(\boldsymbol{m}_{i,j}\cdot\boldsymbol{y}\right)\right)\right) \\ M_{bx} &= \sum_{i=1}^{m}\left(\sum_{j=1}^{l}\left(p_{i,j}\cdot S_{i,j}\cdot\left(\boldsymbol{r}_{i,j}\times\boldsymbol{m}_{i,j}\right)\right)\right) \end{aligned} \tag{9}$$

where l and m are the number of sections of the bridge–wind barrier surface in the ring and longitudinal directions, respectively, and $\boldsymbol{m}_{i,j}$ is the unit normal vector of bridge–wind barrier surface (i, j).

Pressure and aerodynamic load are dimensionless to facilitate quantitative comparative analysis. The calculation formula is expressed as follows:

$$\begin{aligned} C_P &= (P - P_\infty) / (0.5\rho V_a{}^2) \\ C_i &= F_i / (0.5\rho V_a^2 A) \\ C_{mi} &= M_i / (0.5\rho V_a^2 A h) \end{aligned} \tag{10}$$

where P is the aerodynamic pressure acting on the carriage surface; P_∞ is the static pressure at infinity; C_P is the pressure coefficient; C_i (i=y, z) is the aerodynamic force coefficient; C_{mi} (i=x, y, z) is the aerodynamic moment coefficient; F_i (i=y, z) is the aerodynamic force; M_i (i=x, y, z) is the aerodynamic moment; V_a is the resultant wind velocity relative to the train, $V_a = \sqrt{V_w^2 + V_t^2}$, V_w, and V_t are the absolute wind and train speeds, respectively, and A and h are the side area and characteristic height of the carriage, respectively.

3. Verification

3.1. Check of grid independence

Models with different grid sizes are established. The total number of hexahedral mesh elements is 16 million, 32 million and 48million. The number of boundary layers is set to 4, 6, 8, and 10, on the basis of the 32 million grid model, and the maximum lateral force (max-F_z) of three carriages when the train completely running in the bridge with wind barrier is taken as the target index. The other conditions of each model are kept consistent, including crosswind V_w=25 m/s, HSTs V_t=250 km/h, wind barrier H=3 m, porosity α=30%. The corresponding results are shown in Fig. 6. The results show that the max-F_z is completely convergent when the number of boundary layers is 8–10, and the total number of hexahedral mesh elements is 32–48 million. Therefore, 8 layers for the boundary layer and 32 million for the entire mesh in the model are adopted in this study.

3.2. Verification of the porous medium model

Choosing the appropriate pressure loss coefficient model is the key to simplifying the simulation of the porous wind barrier. A corresponding numerical model is established based on the wind tunnel test model of Maruyama (2008). The width (W), height (H), thickness (D) and porosity (α) of the fence wind barrier used in the test are 0.3 m, 0.1 m, 0.006 m and 48%, respectively (Fig. 7(a)).

The size of the calculation zone of the numerical model is 4.5 m×2.0 m×1.0 m. The distance between the wind barrier and the inlet is 1.5 m (Fig. 7(b)). The centre point at the bottom of the wind barrier is set as the origin of coordinates. The incoming flow blows in along the positive direction of the X-axis at a velocity (V_0) of 10 m/s. A boundary layer with 12 grid layers is arranged near the wall of the wind barrier. The thickness of the first grid layer is 1×10^{-4} m. The total number of grid cells in the model is approximately 6 million. The velocity inlet and pressure outlet boundary conditions are used in the inlet and outlet of the model calculation zone, respectively. The DDES turbulence model described in Section 2.1 is still used in the present simulation. The wind barrier zone is set as porous media and simulated using the method described in Section 2.2. In addition, the results of two other reported porous media simulation methods (Hoerner and Bailey models) are also compared (Yeh et al., 2010).

Fig. 8 shows the comparison of the distribution curves of the resultant wind at the position ($X= H$) on Section Z=0 under three pressure loss coefficient models with the corresponding wind tunnel test result. The wind velocity values obtained by the present model (described in Section 2.2) are in good agreement with the test results. The windproof performance of the porous wind barrier adopted in this study can be simulated by the method described in Eq. (8).

3.3. Verification of pressure coefficients

The turbulence model, porous media theory, and relevant calculation methods are verified using the wind tunnel test condition similar to that in this study, that is, the HSTs are on the bridge with wind barrier. On the basis of the wind tunnel test of Central South University, as shown in Fig. 9, a 3D CFD numerical model with the same size as the wind tunnel test of He et al. (2014) is presented.

The wind tunnel test adopts the low-speed test section with a length of 18 m, a width of 12 m and a height of 3.5 m. The wind speed varies within the range of 2-20 m/s, and the corresponding turbulence intensity is less than 2%. A DTC electronic pressure scanning system (Pressure Systems, Inc., USA) was employed to measure the wind pressure. For each measurement, the sampling time was 30 s and the sampling frequency was 330 Hz.

The scale ratio of the model is 1:25, as shown in Fig. 10. The train model is a CRH2 train commonly used in China's high-speed railways, using two carriages (head and middle carriages). The height and width of the train model are 140 mm and 135.2 mm respectively. The head and middle train models are 1028 mm and 1000 mm long respectively. The bridge model is 32 m simply supported box girders, using a five-span bridge model with each span of 1280 mm and the height of bridge pier is 400 mm. The center distance between the two tracks is 200 mm. The wind barrier is 0.1m in height (corresponding to 2.5 m in full scale), the porosity is 30%, the wind speed is 10 m/s, the HSTs speed is 0 km/h, and the wind direction angle is 90°. The same measuring points are arranged in accordance with He’s (2014) model, and the mean pressure coefficient of measuring points 1–9 on the windward side and the top of the middle carriage is taken as the inspection index, as shown in Fig. 11. The total number of model grids is about 4 million. The DDES turbulence model is selected, and the porous wind barrier is simulated by the method described in Section 2.2. The inflow surface is set as the boundary condition of inlet velocity, the outlet is set as the pressure outlet, and the box bridge and train are the smooth walls without sliding.

Table 1. Comparison of pressure coefficient between wind tunnel test and numerical simulation.

Measuring points	1	2	3	4	5	6	7	8	9
Wind tunnel test	-0.22	-0.21	-0.35	-0.43	-1.82	-2.24	-1.28	-1.03	-0.87
Numerical simulation	-0.21	-0.19	-0.38	-0.47	-1.71	-2.36	-1.38	-1.13	-0.80
Relative error (%)	4.5	9.5	8.6	9.3	6.0	5.4	7.8	9.7	8.0

Table 1 shows the comparison of mean pressure coefficients between the wind tunnel test and numerical simulation in different measuring points. The relative error is within 10%. The DDES turbulence model, porous media theory, and calculation method used in this study are reliable.

4. Wind–train–bridge coupled dynamic model

In this study, the transient aerodynamic load of the train and bridge in the bridge and tunnel connected section is inputted into the train–bridge coupled dynamic system to realize the dynamic analysis of running safety. The train–bridge system can be divided into train and track–bridge subsystems. The model of the train–bridge system is shown in Fig. 12.

4.1. Train subsystem

In this study, every carriage of the HSTs is modeled as one carriage body, two bogies, four wheelsets (seven rigid bodies), and primary and secondary suspension systems (as shown in Figs. 12 and 13). The anti-yaw damper has large influence on vehicle dynamic stability. In this paper, the anti-yaw damper adopts the Maxwell model composed of linear stiffness of linear damper in series, which has advantages of more simplified and shorter calculation time on the dynamic simulation of high-speed trains (Alonso et al., 2011; Huang and Zeng, 2018). Every carriage considers 31 DOFs (Deng et al., 2019a), including carriage body and bogie with 5 DOFs (Eqs. (17) and (18)) and wheelset with 4 DOFs (Eq. (19)), without considering the interaction between the carriages.

The dynamic balanced equation of the train subsystem is established (Deng et al., 2019a; Alonso et al., 2011) according to D'Alembert principle, as shown in Eqs. (11) – (19).

$$M_v \ddot{X}_v + C_v \dot{X}_v + K_v X_v = F_v \tag{11}$$

$$F_v = [F_{vc} \;\; F_{vb1} \;\; F_{vb2} \;\; F_{vw1} \;\; F_{vw2} \;\; F_{vw3} \;\; F_{vw4}]^T \tag{12}$$

$$F_{vc} = [F_y - m_{vc} g \;\; F_z \;\; M_x \;\; M_y \;\; M_z]^T \tag{13}$$

$$F_{vbi} = [m_{vb} g \;\; 0 \;\; 0 \;\; 0 \;\; 0]^T (i = 1, 2) \tag{14}$$

$$F_{vwj} = [F_{yj}^{bt} + m_{vw} g \;\; F_{zj}^{bt} \;\; M_{xj}^{bt} \;\; M_{yj}^{bt}]^T (j = 1, 2, 3, 4) \tag{15}$$

$$X_v = [X_{vc} \;\; X_{vb1} \;\; X_{vb2} \;\; X_{vw1} \;\; X_{vw2} \;\; X_{vw3} \;\; X_{vw4}]^T \tag{16}$$

$$X_{vc} = [y_{vc} \;\; z_{vc} \;\; \phi_{vc} \;\; \varphi_{vc} \;\; \psi_{vc}]^T \tag{17}$$

$$X_{vb} = [y_{vbi} \;\; z_{vbi} \;\; \phi_{vbi} \;\; \varphi_{vbi} \;\; \psi_{vbi}]^T (i = 1, 2) \tag{18}$$

$$X_{vw} = [y_{vwj} \;\; z_{vwj} \;\; \phi_{vwj} \;\; \varphi_{vwj}]^T (j = 1, 2, 3, 4) \tag{19}$$

where M_v, C_v and K_v represent the mass, damping, and stiffness matrices of the HSTs subsystem, respectively; F_v represents the vector of external loads on the train subsystem; F_{vc}, F_{vbi}, and F_{vwj} represent the vector of forces on the carriage body, *i*th bogie, and *j*th wheelset; F_z, F_y, M_x, M_y, and M_z represent the aerodynamic loads on the carriage body; F_{yj}^{bt}, F_{zj}^{bt}, M_{xj}^{bt}, and M_{yj}^{bt} represent the forces around *y* and *z* directions and the moments around *x* and *y* directions for the *j*th wheelset on account of track irregularity; m_{vc}, m_{vb}, and m_{vw} represent the mass of the carriage body, bogies and wheelsets; X_v, $\dot{X}_v$, and $\ddot{X}_v$ represent the displacement, velocity, and acceleration vector of the HSTs subsystem, respectively; X_{vc}, X_{vbi}, and X_{vwj} represent the displacement vectors of the carriage body, *i*th bogie, and *j*th wheelset, respectively; y_{vc} and z_{vc} represent the displacement around *y* and *z* directions on the carriage body; y_{vbi} and z_{vbi} represent the displacement around *y* and *z* directions on the *i*th bogie; y_{vwj} and z_{vwj} represent the displacement around *y* and *z* directions on the *j*th wheelset; ϕ_{vc}, φ_{vc}, and ψ_{vc} represent the angles in *x*, *y*, and *z* directions on the carriage body; ϕ_{vbi}, φ_{vbi}, and ψ_{vbi} represent the angles in *x*, *y*, and *z* directions on the *i*th bogie; ϕ_{vwj} and φ_{vwj} represent the angles in *x* and *y* directions on the *j*th wheelset. The detailed formula and the values of the main parameters of the HST subsystem refer to Deng et al. (2019a).

4.2. Track–Bridge subsystem

In this section, a 3D finite element model of the track–bridge is established and 5 DOFs are considered for each bridge unit (Deng et al. 2010a, 2010b, 2019b). While in the tunnel section, the track slab is considered completely fixed. The dynamic balanced equation (as shown in Eqs. (20) – (22)) of the track–bridge subsystem is constructed using a direct stiffness method (Guo et al., 2015b):

$$M_b \ddot{X}_b + C_b \dot{X}_b + K_b X_b = F_b \tag{20}$$

$$F_b = [0 \;\; F_{by} + F_y^{tb} \text{-} m_b g \;\; F_{bz} + F_z^{tb} \;\; M_{bx} + M_x^{tb} \;\; M_y^{tb} \;\; 0]^T \tag{21}$$

$$X_b = [x_b \;\; y_b \;\; z_b \;\; \phi_b \;\; \varphi_b \;\; \psi_b]^T \tag{22}$$

where M_b, C_b, K_b represent the mass, damping, and stiffness matrices of the track–bridge subsystem, respectively, and these coefficients can be directly derived from the finite element model. The detailed formula and values of the main parameters of the track–bridge subsystem can be found in Guo et al. (2015b). X_b, $\dot{X}_b$, and $\ddot{X}_b$ represent the displacement, velocity, and acceleration vector of the track–bridge subsystem, respectively; F_{by}, F_{bz}, and M_{bx} represent the aerodynamic loads on the bridge and wind barrier surface calculated using Eq. (10); F_y^{tb}, F_z^{tb}, M_x^{tb}, and M_y^{tb} represent the wheel–rail interaction force obtained on the basis of the wheel–track interaction model (see Section 4.3); m_b represents the mass of the bridge; x_b, y_b, and z_b represent the displacement along *x*, *y* and *z* directions on the bridge; ϕ_b, φ_b, and ψ_b represent the angles around *x*, *y*, and *z* directions on the bridge.

4.3. Wheel–rail interaction model

The train and track–bridge subsystems are connected with the wheel–rail contact model. Track irregularity includes vertical profile, lateral alignment, cross level and gauge, which is the main excitation source that causes the vibration of the two subsystems. In this study, the German low interference track irregularity spectrum is used as the irregularity excitation of the train–bridge system, because it is conservative in safety analysis. The time history function $x(t)$ of the sinusoidal simple harmonic about track irregularity is stated on the basis of discrete Fourier transform (Deng et al., 2019a), as shown in Eq. (23):

$$x(t)=\sum_{k=1}^{N}\sqrt{2S_x(\omega_k)\Delta\omega}\sin(2\pi\omega_k t+\phi_k) \tag{23}$$

where *N* refers to the total number of samples; $S_x(\omega_k)$ refers to the function of power spectrum density; $\Delta\omega$ refers to the bandwidth of frequency interval; ω_k refers to the frequency; ϕ_k refers to the phase angle; *t* is the time variable.

Hertz nonlinear elastic contact model considering relative deformation of wheel and rail is selected for the wheel–track contact model. The normal wheel–track interaction force F_N is stated as follow:

$$F_N=(\frac{\delta N}{G})^{\frac{3}{2}} \tag{24}$$

where δN is the normal elastic compression, and *G* is the wheel–track contact constant.

The contact velocity of the wheel tread and rail top tread is unequal. Therefore, the effect of spin creep slip rate of wheel and rail should be considered. The creep force is calculated on the basis of the wheel and rail creepage and Kalker’s creep coefficient, as shown in Eq. (25) – (27).

$$F_x^{'} = -\varepsilon f_{11}\zeta_x, \quad F_y^{'} = -\varepsilon(f_{22}\zeta_y + f_{23}\zeta_{sp}), \quad M_z^{'} = \varepsilon(f_{23}\zeta_y - f_{33}\zeta_{sp}) \tag{25}$$

$$\begin{cases} F^{'} = fN\left[\dfrac{F}{fN} - \dfrac{1}{3}\left(\dfrac{F}{fN}\right)^2 + \dfrac{1}{27}\left(\dfrac{F}{fN}\right)^3\right] & \text{for } F \le 3fN \\ F^{'} = fN & \text{for } F > 3fN \end{cases} \tag{26}$$

$$\varepsilon = F^{'}/F \tag{27}$$

where $F_x{'}$, $F_y{'}$, and $M_z{'}$ are the longitudinal creep force, lateral force, and creep moment, respectively, f_{ij} is the creep factor, ε is the correction factor, ζ_x, ζ_y, and ζ_{sp} are the creepages in the longitudinal, lateral, and spin directions, respectively, F is the consultant force of the longitudinal and lateral creep force; $F{'}$ is the consultant force of the revised longitudinal and lateral creep force; N is the normal contact force; f is the friction coefficient of wheel-rail.

4.4. Solution scheme

In this study, the 3D solid numerical model of wind–train–bridge–wind barrier is first built through CFD. The DDES turbulence model is adopted to simulate the flow field structure around the train–bridge system, and the aerodynamic disturbance caused by transverse wind, train wind, and wind barrier is fully considered (mentioned in Sections 2.1-2.5). Then, the time-history data of pressure on the train, bridge, and wind barrier are extracted, and the transient aerodynamic loads of the train and bridge were calculated by using Eqs. (9) – (10) (mentioned in Sections 2.6 and 2.7). Finally, the transient aerodynamic load is inputted into the train–bridge coupled dynamic system (Eqs. (13) and (21)) as the external load to obtain the wheel–track contact force and running safety indexes (DC and WLRR). The dynamic equations of the train and track–bridge subsystems are solved using the Newmark-β method. The separated iterative calculation is compiled on MATLAB platform. The time integral step is 1×10^{-4}s, and the relative error of wheel–track interaction force is 10^{-6} (Deng et al., 2019a), which is taken as the convergence judgment criterion. The calculation flowchart of the wind–train–bridge coupled dynamic system is shown in Fig. 14.

5. Results and discussions

5.1. Aerodynamic coefficient

Fig. 15 shows the time-history curve of the aerodynamic coefficients (C_z, C_y, C_{mx}, C_{my}, and C_{mz}) of each carriage (head, middle, and tail) when the train runs in the bridge and tunnel connected section with or without wind barrier (V_t=250 km/h, V_w=25 m/s, H=3 m, α=30%). Table 2 presents the variation amplitudes of aerodynamic coefficients ($\varDelta C$=Max(C) − Min(C)) of each carriage in the three running processes (‘OUT,’ ‘BR,’ and ‘IN’), and the reduced percentage (RP) and special value ratios are correspondingly listed on the right side of the table. ‘OUT’ represents the process from the nose tip of the head car leaving the tunnel to the nose tip of the tail car entering the bridge (t=4.03–5.13 s) “BR” denotes that all carriages completely run in the bridge (t=5.13–6.32 s). ‘IN’ refers to the process from the nose tip of the head car entering the tunnel to the nose tip of the tail car leaving the bridge (t=6.32–7.42 s).

Table 2. Comparison of the variation amplitudes of aerodynamic coefficients with or without wind barrier.

Index	Carriage	OUT Max(C)-Min(C) Without	OUT Max(C)-Min(C) With	OUT RP (%)	IN Max(C)-Min(C) Without	IN Max(C)-Min(C) With	IN RP (%)	BR Max(C)-Min(C) Without	BR Max(C)-Min(C) With	BR RP (%)	Specific value With barrier $\Delta C_{OUT}/\Delta C_{IN}$	Specific value With barrier $\Delta C_{OUT}/\Delta C_{BR}$
C_z	Head	0.360	0.040	89	0.374	0.042	89	0.023	0.015	35	0.95	2.67
	Middle	0.379	0.023	94	0.374	0.028	92	0.015	0.014	6.7	0.82	1.64
	Tail	0.309	0.036	88	0.362	0.036	91	0.068	0.025	63	1.00	1.44
C_y	Head	0.182	0.025	86	0.132	0.017	87	0.029	0.019	34	1.47	1.32
	Middle	0.090	0.042	53	0.105	0.035	67	0.008	0.010	-25	1.20	4.20
	Tail	0.102	0.018	82	0.148	0.014	91	0.040	0.013	68	1.29	1.38
C_{mx}	Head	0.052	0.006	89	0.055	0.006	89	0.003	0.002	33	1.00	3.00
	Middle	0.055	0.003	94	0.055	0.004	92	0.002	0.002	0	0.75	1.50
	Tail	0.045	0.005	88	0.053	0.005	91	0.010	0.004	60	1.00	1.25
C_{my}	Head	0.317	0.121	62	0.279	0.121	57	0.059	0.022	63	1.00	5.50
	Middle	0.244	0.041	83	0.226	0.022	90	0.015	0.014	6.7	1.86	2.93
	Tail	0.308	0.069	78	0.311	0.032	90	0.065	0.050	23	2.16	1.38
C_{mz}	Head	0.104	0.077	52	0.159	0.053	67	0.025	0.027	-8	1.45	2.85
	Middle	0.087	0.031	64	0.173	0.032	81	0.009	0.011	-22	0.97	2.82
	Tail	0.082	0.037	55	0.152	0.038	75	0.067	0.020	70	0.97	1.85

Niu et al. (2014) found that the windward slope of the hill causes the airflow to accelerate; on the leeward slope, the airflow velocity decreases because of the mountain obstruction; and the acceleration of air between the two mountains results in throttling. Accordingly, the distribution of wind velocity along the longitudinal direction of the bridge is actually asymmetric under the combined action of narrow channel effect and terrain in the canyon. Even so, Niu et al. (2014) argued that the variation of wind velocity value on the bridge is still limited. The peak wind velocity is only 1.34 times of the mean value under the condition of incoming wind velocity of 25 m/s. Thus, the wind field set in this paper is an idealized extreme condition. The following findings were obtained from Fig. 15 and Table 2:

In the bridge–tunnel section (including the ‘OUT’ and ‘IN’), a significant sudden change effect was found on the aerodynamic coefficient without wind barrier. The sudden change effect significantly decreased by more than 50% once the wind barrier was installed (columns 5 and 8 in Table 2). The coefficients of lateral force and rolling moment evidently decreased, reaching more than 88%. The variation amplitudes of the lateral force coefficient (ΔC_z) of the head, middle, and tail carriage decreased by 89%, 94%, and 88%, respectively in the ‘OUT’ process and by 89%, 92%, and 91%, respectively, in the ‘IN’ process. The sensitivity of pitching moment coefficient affected by wind barrier was relatively weaker, with a drop of 52%–81%.

In the bridge section (“BR”), the variation amplitudes of aerodynamic coefficient of each carriage reduced by 6.7%–70% after setting the wind barrier. The ΔC_z values of the head, middle, and tail carriages decreased by 35%, 6.7%, and 63%. These values were 54%, 87.3%, and 25% lower than the ‘OUT’ process and 54%, 85.3%, and 28%

lower than the ‘IN’ process respectively. The sensitivity of wind barrier to the sudden change effect of aerodynamic coefficient in the bridge section was obviously weaker than that in bridge–tunnel section.

The ΔC values of each carriage in the bridge–tunnel section (‘OUT’ or ‘IN’) were evidently higher than the corresponding values in the bridge section with wind barrier. The ΔC values of each carriage in the ‘OUT’ process were 1.25 to 5.5 times higher than that the corresponding values in the bridge section, whereas those in the ‘OUT’ and ‘IN’ processes were basically the same (columns 9 and 10 in Table 2). The ΔC_z values of the head, middle, and tail carriage in the ‘OUT’ process were 2.67, 1.64, and 1.44 times of the bridge section, which were 0.95, 0.82, and 1.00 times of the ‘IN’ process.

5.2. Flow field structure and pressure coefficient

Figs. 16 and 17 show the flow field of the typical cross-sections when the half of the carriage leaving the tunnel (‘OUT’) and entering the tunnel (‘IN’), respectively. The distance between the cross-section and the tunnel entrance is ±10 m. The following findings were obtained from Fig 16.

In the tunnel, the pressure coefficient of the carriage was basically uniform and symmetrical in the transverse direction whether with or without wind barrier, and the pressure difference was basically zero, which are negative pressure. However, the negative pressure of the carriage with wind barrier was large, as shown in Fig. 16(c_1). This finding was caused by the difference in the location of the vortex structure under the two conditions, as shown in Figs 16 (a_1) and (b_1).

For the bridge without wind barrier (as shown in Figs. 16 (a_3) and (c_3)), the windward side of the carriage was directly impacted by crosswind and was under positive pressure. The bottom and top of the train carriage were under negative pressure because of the surrounding flow. The surrounding flow was significant at the intersection of the windward side and the roof, and the negative pressure was large. The airflow separation on the leeward side resulted in negative pressure. The above phenomenon led to a large pressure difference of the carriage in the transverse direction. The distribution difference of flow field structure and pressure coefficient between the tunnel and the bridge without wind barrier resulted in a large pressure difference in the longitudinal direction on the two sides of the carriage. Therefore, a significant aerodynamic abrupt effect of the HSTs was found in the ‘OUT’ process.

For the bridge with wind barrier (as shown in Fig. 16 (b_3) and (c_3)), the direct impact of crosswind on the windward side of the carriage was weakened because of the obstruction and diversion of the wind barrier. The space on the windward side was limited, and the influence of train wind was dominant, resulting in the pressure of the HSTs on the windward side from positive to negative. The vortex structure on the leeward side expanded in scope and reduced in intensity because of the two-time shunting effect of the wind barrier and the train. Accordingly, the negative pressure of the HSTs on the leeward side reduced. The pressure difference between the two sides of the carriage evidently decreased. The distribution form of the pressure coefficient in the bridge segment was similar to that in the tunnel. Therefore, the longitudinal distribution difference of the pressure difference between the two sides of the carriage was remarkably reduced (the pressure difference is reduced between the tunnel and the bridge), and the corresponding fluctuation amplitudes of the aerodynamic coefficient were significantly decreased. These phenomena are also fully reflected in Fig.17, which again guarantees the reliability of the above analysis.

Under the condition without crosswind and wind barrier, the flow field at the two sides of the train is mainly a circumferential flow centred on the train that flowed from the front of the leading carriage to the rear of the tail carriage. Once the HST entering tunnel, a squirt flow opposite to the train running direction will be generated in the gap between the carriage and tunnel wall at the tunnel entrance due to the combined action of instantaneous extrusion of stationary air within the tunnel and original circumferential flow on the two sides of the train. The difference in Fig. 17 is that the pressure coefficient values of the underbody and leeward side are larger under condition without wind barrier. This finding was caused by obvious squirt flow generated from the 'IN' process. Accordingly, the strength of the vortex structure under the leeward side was enhanced and the negative pressure was increased (Figs. 17 (a_1) and (c_1)).

5.3. Runninng safety

As shown in Table 2 in Section 5.1, the fluctuation amplitudes of aerodynamic coefficient of the head carriage are greater than those of the middle and tail carriage, which is consistent with the research conclusion in Yang et al. (2019) and Deng et al. (2019a). This section considers the running safety of the head carriage as an example to study the influence of wind barrier on DC and WLRR and the influence of different wind and train speeds.

5.3.1. Derailment coefficient

On the basis of the TB10621-2009, the safety criterion of the DC for the HSTs in the bridge and tunnel connection section is expressed as follows:

$$Q / P \leq 0.8 \tag{28}$$

where Q and P are the lateral and vertical forces acting on the wheels, respectively.

Fig. 18 shows the time history curves of the DC of each wheelset in the head carriage with and without wind barrier (Vt=250 km/h, Vw=25 m/s, H=3 m, and α=30%). Fig. 19 shows the maximum peaks of DC for the first and third wheelsets under different running processes ('OUT,' 'BR,' and 'IN'). The following findings were obtained from Figs 18 and 19:

In the bridge section ("BR"), the DC of each wheel on the leeward side immensely fluctuated, and an obvious sudden increase phenomenon without wind barrier was observed. The maximum peaks of the first and third wheelsets on the leeward side were 1.22 and 0.93, respectively (as shown in Fig. 19). However, the DC on the windward side oscillated within 0.2. After setting the wind barrier, the maximum peaks of DC for each wheel was significantly reduced and vibrated within the range of 0.2. The running safety was high, indicating that the protection effect of the wind barrier with the height of 3 m and porosity of 30% is better in the bridge section.

The above phenomena can be explained in accordance with the aerodynamic load and movement postures of the HSTs in Fig. 15. The carriage inclines to the leeward side under the action of rolling moment, resulting in close contact between the wheel and rail on the leeward side without wind barrier. The DC value immensely fluctuates and abruptly increases because of the action of track irregularity. However, the carriage pressure is evenly distributed (as shown in Figs 16(c_3) and 17(c_1)) with wind barrier, the aerodynamic load and the effect of aerodynamic fluctuation is small, and the HSTs stably operates without abruptly increasing the DC.

In the bridge–tunnel section ('OUT' and 'IN'), a sudden increase was found in the DC value of the first and third wheelsets with wind barrier. In the 'OUT' process, the first and third wheelsets on the leeward side abruptly increased, with peak values of 0.71 and 0.44, respectively. On the contrary, in the 'IN' process, a sudden increase was found in the first and third wheelsets on the windward side, with a peak value of 0.37. This condition is probably because the first and third wheelsets are located in the front wheels of the bogie of the head car, thereby causing close contact and collision between the wheel tread and the top surface of the track. In the 'OUT' process, the train is suddenly impacted by the crosswind, and the carriage tilts to the leeward side. The wheels and tracks produce an instantaneous impact on the leeward side, and the DC suddenly increases. In the 'IN' process, the lateral force and rolling moment on the carriage are abruptly unloaded after entering the tunnel. The carriage restores to the equilibrium position, and the wheel and track on the windward side produce an instantaneous impact.

The sensitivity of the DC for the bridge–tunnel and bridge sections to the impact of the wind barrier is different, and the bridge–tunnel section is the weak link of running safety control in the entire running process.

5.3.2. Wheel load reduction rate

The WLRR is also an important index in the safety judgment of train running. The lateral force of the HSTs is extremely small (or not), the wheel load is reduced because of the up-down vibration of the wheel, and derailment may occur because of the lateral relative displacement. WLRR is selected as another safety index to evaluate running safety. In this study, the evaluation criteria of the WLRR studied by Zhai and Chen (2001) are adopted, as shown in Eq. (29).

$$\begin{cases} \Delta P / P \le 0.80 \\ \Delta P / P > 0.80,\ \Delta t < 0.035s \end{cases} \tag{29}$$

where ΔP is the load reduction of wheel load, P is the average static wheel load of each wheelset, and Δt is the maximum overrun duration.

Fig. 20 shows the time history curves of the WLRR of each wheelset in the head carriage with and without wind barrier (V_t=250 km/h, V_w=25 m/s, H=3 m, and α=30%). Fig. 21 shows the maximum duration of WLRR overrun of the first and third wheelsets for different running processes. The following findings were obtained from Figs. 20 and 21:

The WLRR time history curves of the head car with and without wind barrier are compared with the three processes of 'OUT,' 'BR,' and 'IN'. Without wind barrier, as shown in Fig. 20(a), where Δt is0.04, 0.04, and 0.02 s, respectively (as shown in Fig. 21). After setting the wind barrier, the variation range of WLRR for each wheelset in the three running processes is evidently reduced. However, the 'OUT' process has a sudden enhancement effect (Δt is 0.01 s), whereas the processes of 'IN' and 'BR' have no phenomenon of fluctuation exceeding the limit. This finding shows that the 'OUT' process (or the bridge–tunnel section) is the weakest link of safety control in the entire running process of the HSTs, which is consistent with the conclusion in Section 5.3.1.

5.3.3. Effects of train speeds and crosswind velocities

In this section, DC is taken as the main safety index. The influences of different train and crosswind speeds about the safety index of DC at the bridge–tunnel and bridge sections are analyzed under the condition of wind barrier (H=3 m and α=30%). The maximum peaks of DC in different running process under different HSTs and crosswind speeds with wind barriers are shown in Fig. 22.

The maximum peaks of DC fluctuation occur in the first and third wheelsets under different train and crosswind speeds. The 'OUT' process appears on the leeward side, and the 'IN' process appears on the windward side (consistent with the phenomenon in Section 5.3.1).

The maximum peaks of DC fluctuation in the bridge–tunnel section ('OUT' or 'IN') are greater than that in the bridge section under different conditions. This finding shows that the running safety of the bridge–tunnel section is lower under the same wind barrier parameters and plays a safety control role in the entire running process. Adopting a wind barrier with the same parameters for the bridge–tunnel section as for the bridge section is unreasonable. The optimal parameters of the wind barrier in the bridge–tunnel section, including the height, porosity, and setting length of the wind barrier, should be separately designed to improve the running safety of the bridge–tunnel connection section.

6. Conclusions

In this study, the 3D CFD numerical model of the train–tunnel–bridge–wind barrier system is presented, and the dynamic analysis model of wind–train–bridge coupling is combined to realize the dynamic analysis of running safety. The influences of wind barrier on the aerodynamic coefficient, flow field structure, and running safety of HSTs in the bridge–tunnel section are studied. The results of numerical simulation are in good agreement with those of wind tunnel test. The conclusions are summarized as follows:

(1) Aerodynamic coefficient

The abrupt effect of aerodynamic coefficient in the bridge–tunnel section (‘OUT’ and ‘IN’) is significantly weakened by setting the wind barrier, with a reduction of more than 50%. The reduction in lateral force and rolling moment coefficient is more than 88%, and the reduction in pitching moment coefficient is between 52% and 81%. The variation amplitudes of aerodynamic coefficient in the ‘OUT’ and ‘IN’ processes are basically the same, which is significantly larger than that in the bridge section. The variation amplitudes of aerodynamic coefficient in the ‘OUT’ process are 1.25–5.5 times higher than those in the bridge section.

(2) Flow field structure and pressure coefficient

The flow field structure changes, the difference about pressure on the two sides of the carriage is significantly reduced because of the obstruction and diversion of the wind barrier and the space limitation on the windward side, and the influence of train wind is dominant. Thus, the difference about pressure distribution in the longitudinal direction (in the tunnel and on the bridge) is significantly reduced. Therefore, the abrupt effect of aerodynamic coefficient in the bridge–tunnel section is significantly decreased.

(3) Running safety

The wind barrier can significantly reduce the safety index and improve the running safety under strong crosswind. The running safety index of the bridge–tunnel section abruptly increases with wind barrier, which is the weak link of safety control. The sensitivity of the bridge–tunnel and bridge sections to the parameters of the wind barrier is different, that is, the optimal parameters of the wind barrier are different. Adopting the same parameters of wind barrier for the bridge–tunnel section as the bridge section is unreasonable. Thus, the design parameters should be separately optimized.

Although a preliminary idea for the optimal design of wind barriers in the bridge–tunnel section is proposed in the present study, numerous model and field tests are still required to acquire specific optimisation design parameters such as the length and the transition form from the bridge-tunnel section to the bridge section. Next step, the authors will do further researches for the issue mentioned above.

CRediT authorship contribution statement

Weichao Yang: Conceptualization, Investigation, Writing-review & editing. **E Deng**: Methodology, Software, Writing-original draft. **Xuhui He**: Funding acquisition, Validation, Writing-review & editing. **Zhihui Zhu**: Resources, Writing-review & editing. **Ang Wang**: Data curation, Investigation. **Zhao Wen**: Writing-review & editing.

Acknowledgment

This work was funded by the National Natural Science Foundation of China (Grant Nos. 51978670 and U1534206) and the Fundamental Research Funds for the Central Universities of Central South University (Grant No. 2019zzts291). The authors are grateful for the supports awarded. In addition, the authors would like to thanks Ms. Xinyang Li for her great support for this paper.

References

Alonso, A., Giménez, J.G., Gomez, E., 2011. Yaw damper modelling and its influence on railway dynamic stability. Veh. Syst. Dyn. 49(9), 1367–1387.

Avila-Sanchez, S., Lopez-Garcia, O., Cuerva, A., Meseguer, J., 2016. Characterisation of cross-flow above a railway bridge equipped with solid windbreaks. Eng. Struct. 126, 133-146.

Deng, E., Yang, W.C., Deng, L., Zhu, Z.H., He, X.H., Wang, A., 2020a. Time- resolved aerodynamic loads on high-speed trains during running on a tunnel–bridge–tunnel infrastructure under crosswind. Eng. Appl. Comput Fluid Mech. 14(1), 202–221.

Deng, E., Yang, W.C., He, X.H., Ye, Y.C., Zhu, Z.H., Wang, A., 2020b. Transient aerodynamic performance of high-speed trains passing through an infrastructure consisting of tunnel-bridge-tunnel under crosswind. Tunn. Undergr. Sp. Technol. 102, 103440.

Deng, E., Yang, W.C., Lei, M.F., Zhu, Z.H., Zhang, P.P., 2019a. Aerodynamic loads and traffic safety of high-speed trains when passing through two windproof facilities under crosswind: A comparative study. Eng. Struct. 188, 320-339.

Deng, L., Cai, C.S., 2010a. Development of dynamic impact factor for performance evaluation of existing multi-girder concrete bridges. Eng. Struct. 32(1), 21-31.

Deng, L., Cai, C.S., 2010b. Bridge model updating using ressponse surface method and genetic algorithm. J. Bridge Eng. (ASCE) 15(5), 553-564.

Deng, L., Yan, W.C., Nie, L., 2019b. A simple corrosion fatigue design method for bridges considering the coupled corrosion-overloading effect. Eng. Struct. 178, 309-317.

Guo, W.W., Wang, Y.J., Xia, H., Lu, S., 2015a. Wind tunnel test on aerodynamic effect of wind barriers on train-bridge system. Science China Technological Sciences 58(2), 219-225.

Guo, W.W., Xia, H., Karoumi, R., Zhang, T., Li, X.Z., 2015b. Aerodynamic effect of wind barriers and running safety of trains on high-speed railway bridges under cross winds. Wind Struct. 20(2), 213-236.

He, X.H., Shi, K., Wu, T., Zou, Y.F., Wang, H.F., Qin, H.X., 2016. Aerodynamic performance of a novel wind barrier for train-bridge system. Wind Struct. 23(3), 2-20.

He, X.H., Zou, Y.F., Wang, H.F., Han, Y., Shi, K., 2014. Aerodynamic characteristics of a trailing rail vehicles on viaduct based on still wind tunnel experiments. J. Wind Eng. Ind. Aerodyn. 135, 22-33

Huang, C.H. Zeng, J., 2018. Dynamic behaviour of a high-speed train hydraulic yaw damper. Veh. Syst. Dyn. 56(12), 1922-1944

Kozmar, H., Procino, L., Borsani, A., Gianni, B., 2014. Optimizing height and porosity of roadway wind barriers for viaducts and bridges. Eng. Struct. 81, 49-61.

Li, Y.L., Qiang, S.Z., Liao, H.L., Xu, Y.L., 2005. Dynamics of wind-rail vehicle-bridge systems. J. Wind Eng. Ind. Aerod. 93(6), 483–507.

Li, T., Yu, M.G., Zhang, J.Y., Zhang W.H., 2015. A fast equilibrium state approach to determine interaction between stochastic crosswinds and high-speed trains. J. Wind Eng. Ind. Aerodyn. 143, 91–104.

Li, T., Qin D., Zhang, J.Y., 2019. Effect of RANS turbulence model on aerodynamic behavior of trains in crosswind. Chinese Journal of Mechanical Engineering 32, 85.

Liu, T.H., Chen, Z.W., Zhou, X.S., Zhang, J., 2017. A CFD analysis of the aerodynamics of a high speed train passing through a windbreak transition under crosswind. Eng. Appl. Comput Fluid Mech. 12(1), 137–51.

Lu, Y.B., Wang, T.T., Yang, M.Z., Qian, B.S., 2020. The influence of reduced cross-section on pressure transients from high-speed trains intersecting in a tunnel. J. Wind Eng. Ind. Aerodyn. 201, 104161.

Maruyama, T., 2008. Large eddy simulation of turbulent flow around a windbreak. J. Wind Eng. Ind. Aerodyn. 96, 1998–2006.

Montenegro, P.A., Carvalho, H., Calçada, R., Bolkovoy, A, Chebykin, I., 2019. Stability of a train running over the Volga River high-speed railway bridge during crosswinds. Structure and Infrastructure Engineering. 11, 1-17.

Niu, J.Q., Zhou, D., Li, Z.W., Yang, M.Z., 2014. Research on aerodynamic performance of high-speed train through canyon wind zone. Journal of the China Railway Society 36(6), 9-14 (in Chinese).

Niu, J.Q., Zhou, D., Liang, X., Liu, T., Liu, S., 2017a. Numerical study on the aerodynamic pressure of a metro train running between two adjacent platforms. Tunn. Undergr. Space Technol. 65, 187–99.

Niu, J.Q., Zhou, D., Liu, T.H., Liang, X.F., 2017b. Numerical simulation of aerodynamic performance of a couple multiple units high-speed train. Veh. Syst. Dyn. 55(5), 681–703.

Niu, J.Q., Zhou, D., Wang, Y., 2018. Numerical comparison of aerodynamic performance of stationary and moving trains with or without windbreak wall under crosswind. J. Wind Eng. Ind. Aerodyn. 182, 1-15.

Olmos, J.M., Astiz, M.A., 2018a. Improvement of the lateral dynamic response of a high pier viaduct under turbulent wind during the high-speed train travel. Eng. Struct. 165, 368-385.

Olmos, J.M., Astiz, M.A., 2018b. Non-linear vehicle-bridge-wind interaction model for running safety assessment of high-speed trains over a high-pier viaduct. Journal of Sound and Vibration. 419, 63-89.

Paz, C., Suarez, E., Gil, C., 2017. Numerical methodology for evaluating the effect of sleepers in the underbody flow of a high-speed train. J. Wind Eng. Ind. Aerodyn. 167, 140-147.

TB10621-2009. Code for Design of High-Speed Railway. China Railway Publishing House, Beijing, China. (in Chinese)

Wang, T.T., Wu, F., Yang M.Z., Ji, P., Qian B.S., 2018. Reduction of pressure transients of high-speed train passing through a tunnel by cross-section increase. J. Wind Eng. Ind. Aerodyn. 183, 235-242.

Wei, L., Zeng, J., Wu P.B., Song, C.Y, 2018. Safety analysis of high speed trains under cross winds using indirect wheel-rail force measuring method. J. Wind Eng. Ind. Aerodyn. 183, 55-67.

Xia, H., Guo, W.W., Zhang, N., Sun, G.J., 2008. Dynamic analysis of a train-bridge system under wind action. Comput. Struct. 86, 1845-1855.

Xiang, H.Y., Li, Y.L., Chen, B., Liao, H.L., 2014. Protection effect of railway wind barrier on running safety of train under cross winds. Adv. Struct. Eng. 2014, 17(8), 1177-1187.

Yeh, C.P., Tsai, C.H., Yang, R.J., 2010. An investigation into the sheltering performance of porous windbreaks under various wind directions. J. Wind Eng. Ind. Aerodyn. 98, 520-532.

Yang, W.C., Deng, E., Lei, M.F., Zhang, P.P., Yin, R.S., 2018. Flow structure and aerodynamic behavior evolution during train entering tunnel with entrance in crosswind. J. Wind Eng. Ind. Aerodyn. 175, 229–243.

Yang, W.C., Deng, E., Lei, M.F., Zhu, Z.H., Zhang, P.P., 2019. Transient aerodynamic performance of high-speed trains when passing through two windproof facilities under crosswinds: A comparative study. Eng. Struct. 188, 729-744.

Yang, W.C., Deng, E., Zhu, Z.H., Lei, M.F., Shi, C.H., He, H., 2020. Sudden variation effect of aerodynamic loads and safety analysis of running trains when entering tunnel under crosswind. Appl. Sci. 10(4), 1445.

Zhai, W.M., Chen, G., 2001. Method and criteria for evaluation of wheel derailment based on wheel vertical rise. Journal of the China Railway Society. 02, 17-26. (in Chinese).

Zhang, T., Xia, H., Guo, W.W., 2013. Analysis on running safety of train on bridge with wind barriers subjected to cross wind. Wind Struct. 17, 203-225.

Zou, S.M., He, X.H., Wu, T., Zou, Y.F., Jing, H.Q., 2018. Numerical simulation of aerodynamic characteristics of Wind-Vehicle-Bridge system. I. C. R. T 2017. 789-797.

Figure

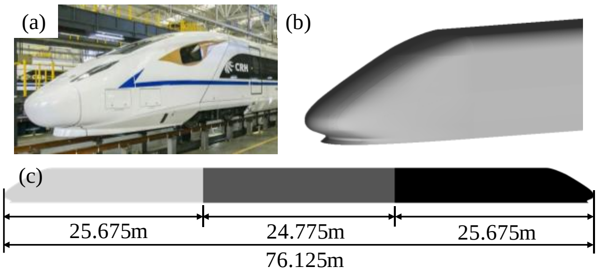

Fig. 1. Comparison of (a) HST's prototype and (b-c) HST's numerical model.

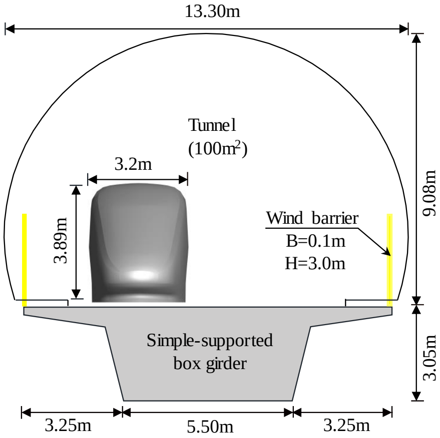

Fig. 2. Geometric models of Bridge, tunnel and wind barrier.

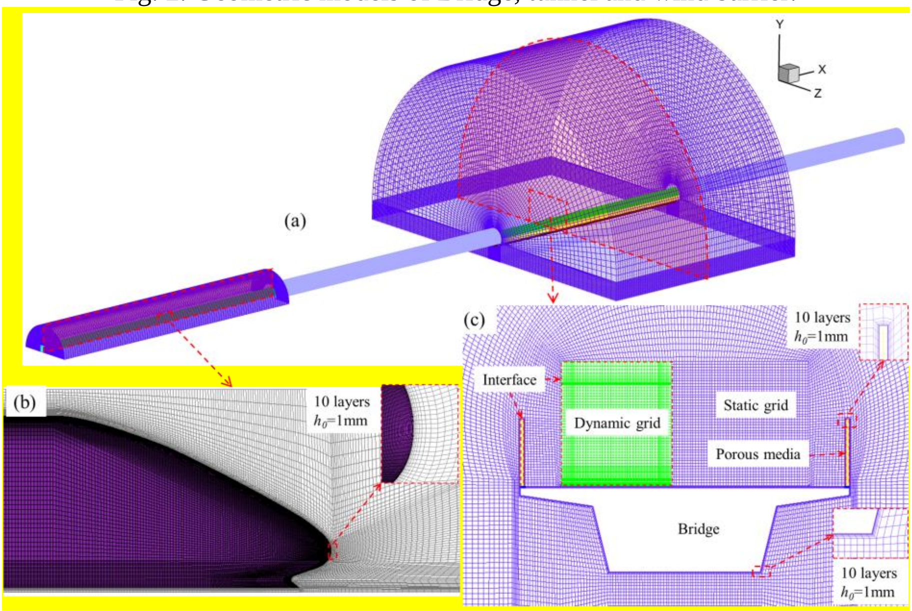

Fig. 3. Grid model: (a) the whole grid, (b) the grid at train nose and (c) the grid at bridge section.

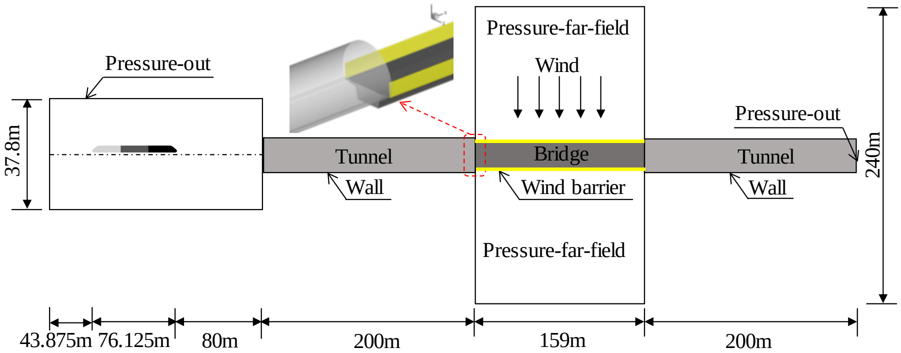

Fig. 4. Boundary conditions.

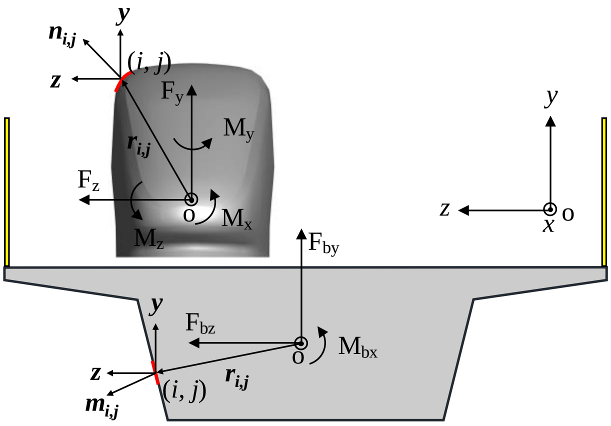

Fig. 5. Schematic diagram of HST and bridge aerodynamic loads.

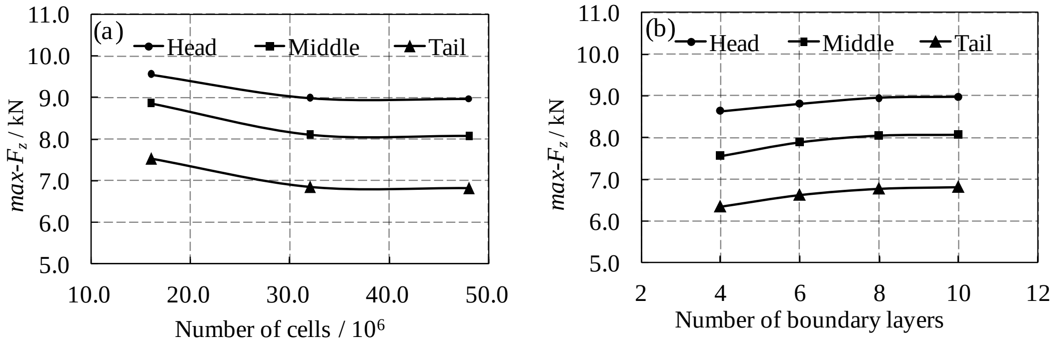

Fig. 6. The test of grid independence: (a) grid resolution and (b) boundary layer.

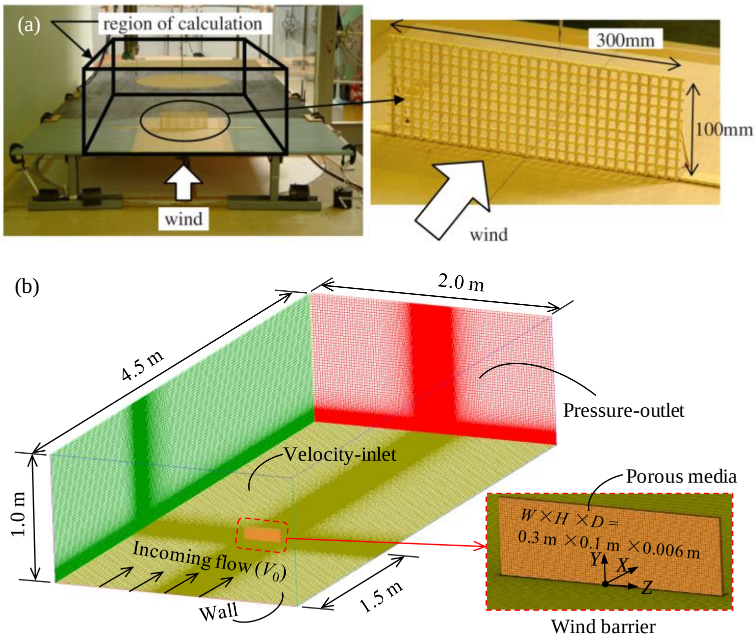

Fig. 7. Comparison of models: (a) Maruyama's wind tunnel test model and (b) the corresponding CFD numerical model.

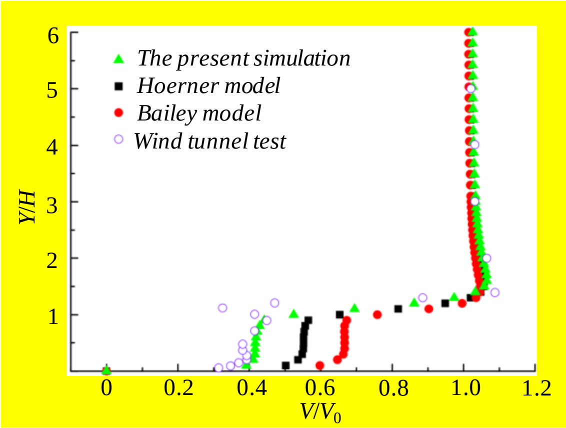

Fig. 8. Comparison of wind velocity results.

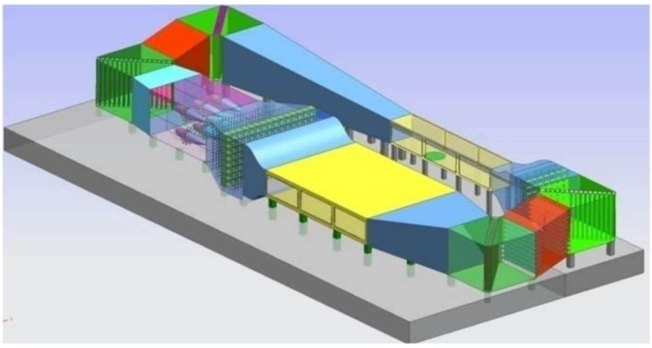

Fig. 9. Schematic diagram of the wind tunnel laboratory of Central South University

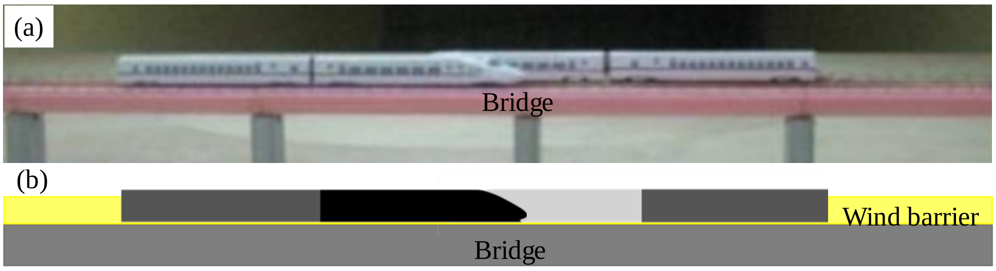

Fig. 10. Comparison of (a) wind tunnel test model and (b) numerical simulation model.

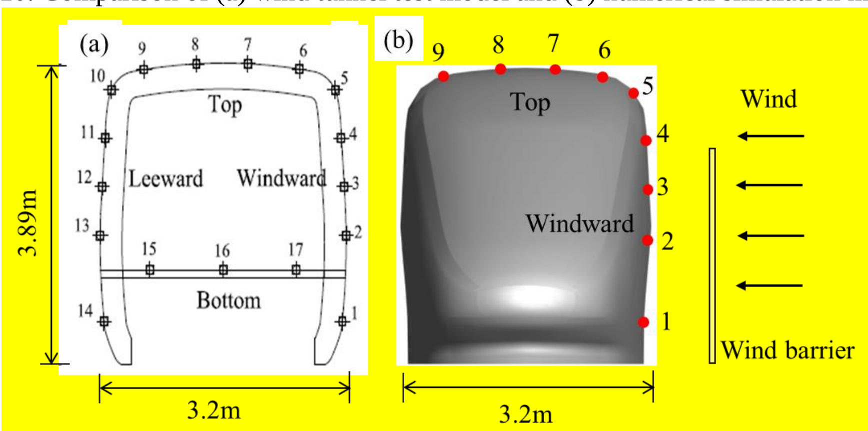

Fig. 11. The arrangement of measuring points on the train: (a) wind tunnel test and (b) numerical simulation.

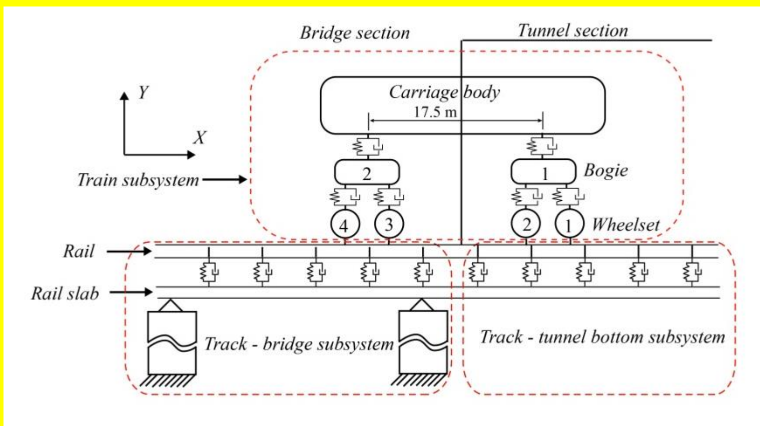

Fig. 12. Wind-train-bridge coupled dynamic model.

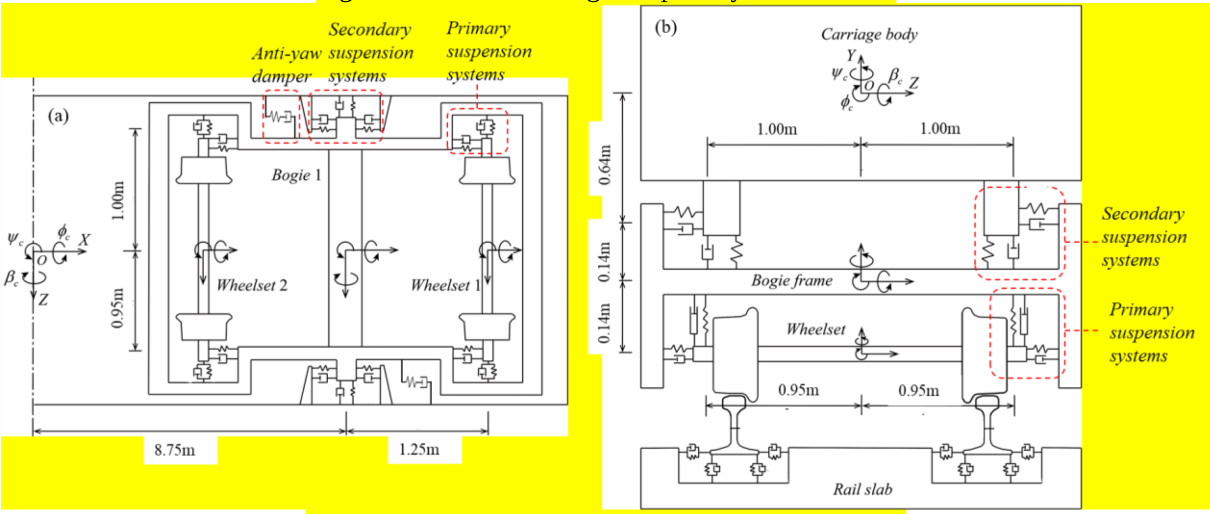

Fig. 13. HSTs model: (a) plan view and (b) end view.

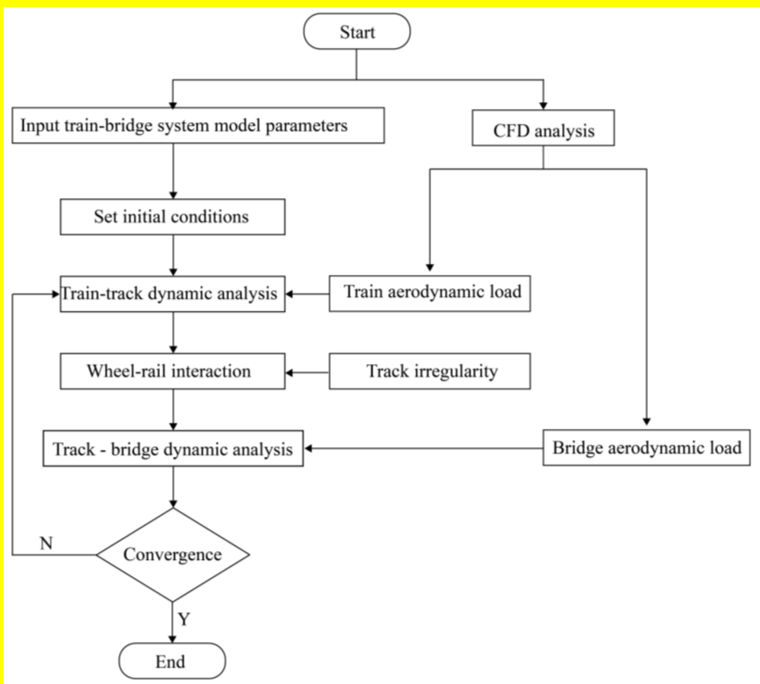

Fig. 14. Calculation flowchart of wind-train-bridge coupled dynamic system.

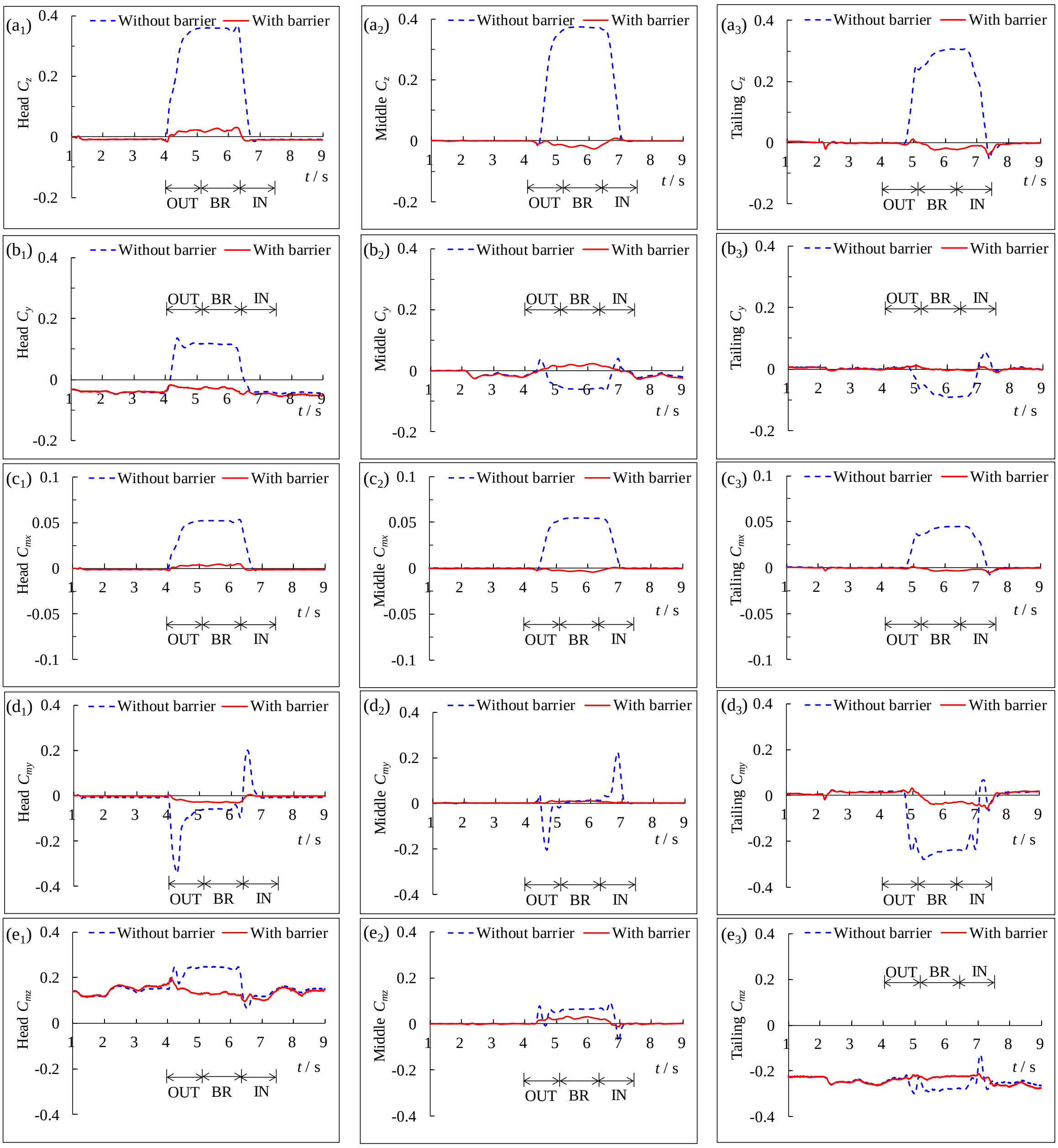

Fig. 15. Comparison of aerodynamic load coefficients of the HSTs with or without wind barrier: (a) Transverse force; (b) Lift force; (c) Rolling moment; (d) Yawing moment and (e) Pitching moment.

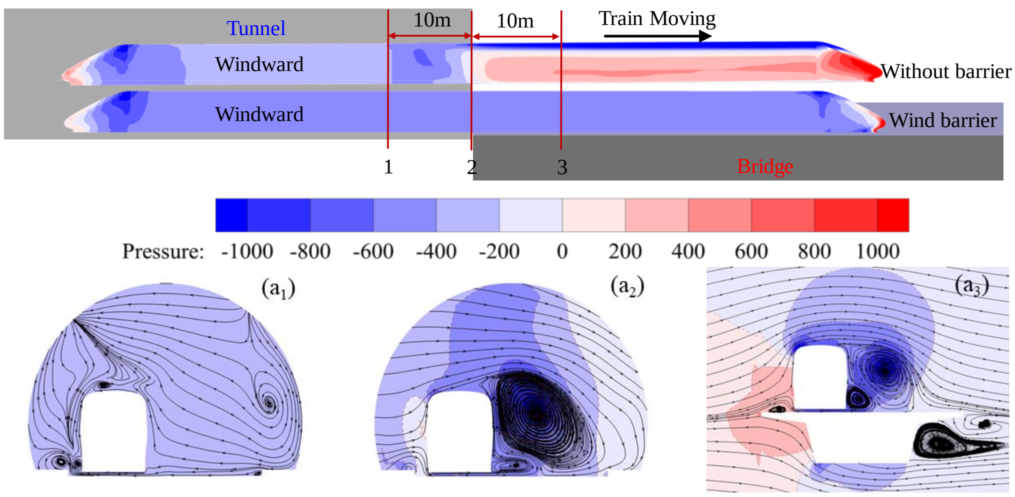

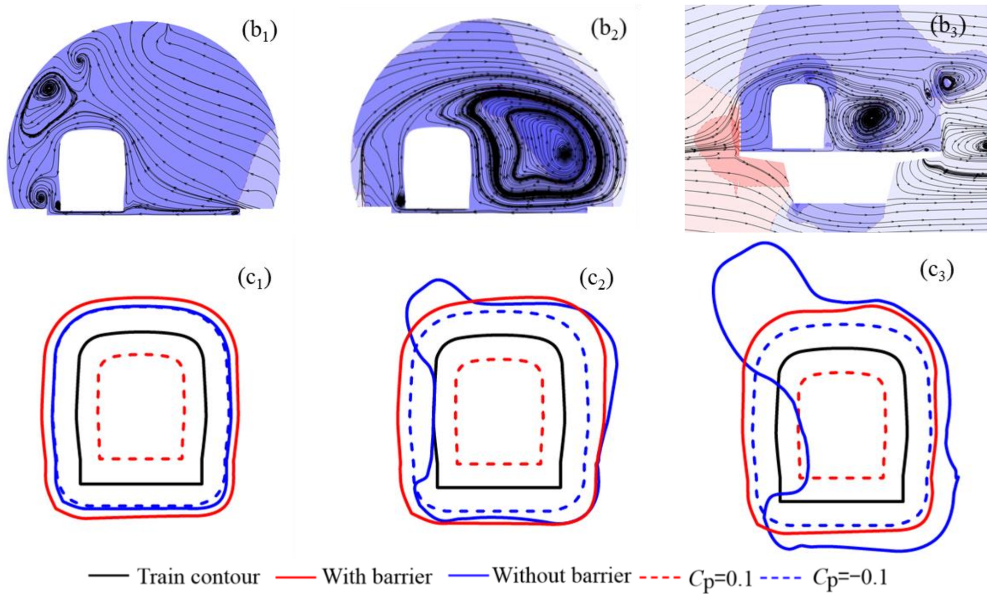

Fig. 16. Flow field structure and pressure coefficient diagram of the carriage leaving the tunnel halfway: (a) Without wind barrier; (b) With wind barrier and (c) Pressure coefficient diagram.

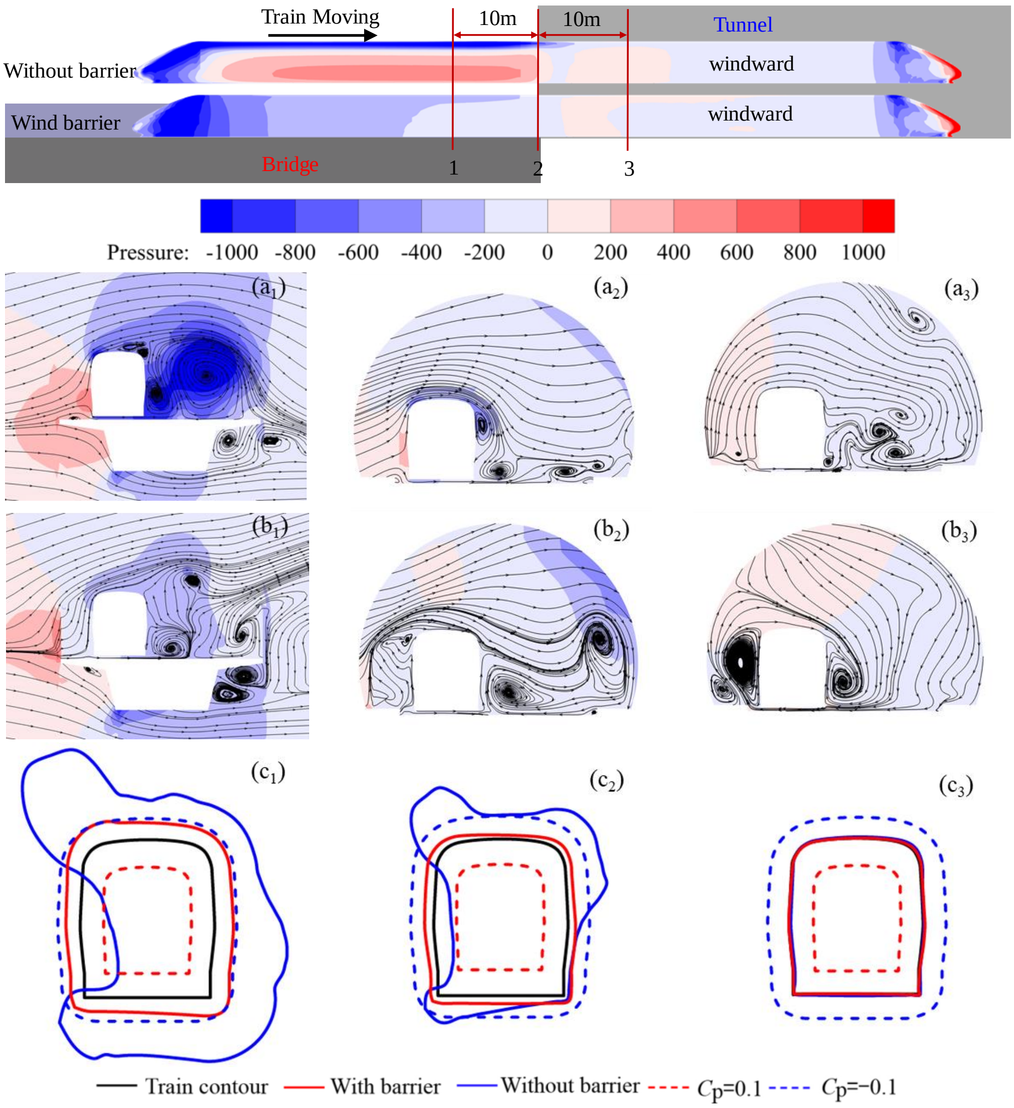

Fig. 17. Flow field structure and pressure coefficient diagram of the train carriage entering the tunnel halfway: (a) Without wind barrier; (b) With wind barrier and (c) Pressure coefficient diagram..

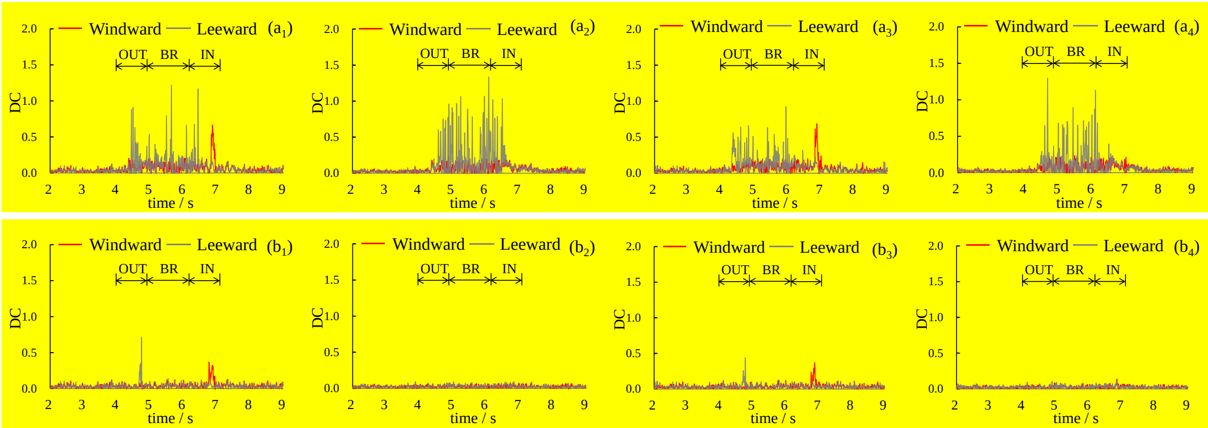

Fig. 18. Time history curve of head DC with or without wind barrier: (a_i) Without wind barrier and (b_i) With wind barrier ; The subscript *i* =1-4 , respresents the ith wheelsets.

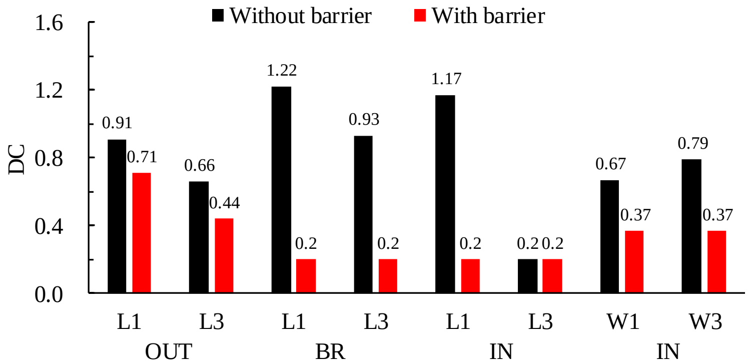

Fig. 19. The DC peaks of the first and third wheelsets in different running processes (W*i* and L*i* are the *i*th wheelset on the windward side and leeward side respectively, *i* = 1,3).

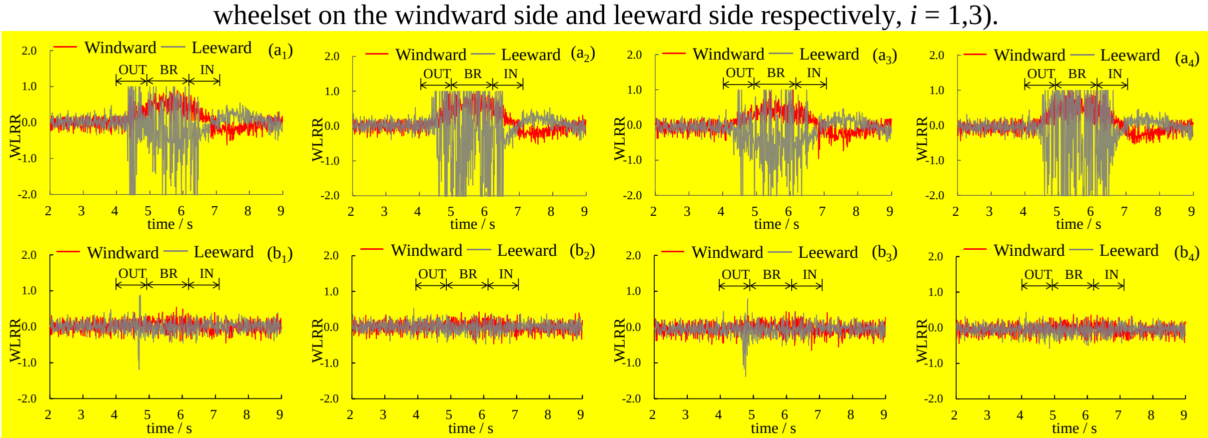

Fig. 20. Time-history curves of WLRR with or without wind barrier: : (a_i) Without wind barrier and (b_i) With wind barrier ; The subscript *i* =1-4 , respresents the ith wheelsets..

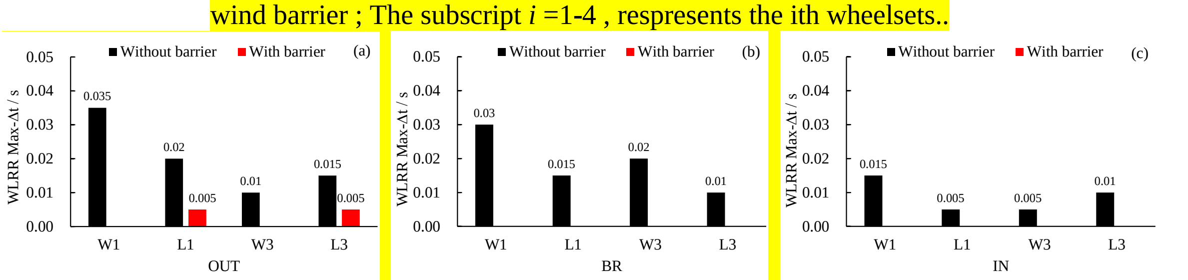

Fig. 21. the maximum duration of WLRR overrun of the first and third wheelset for different running processes (W*i* and L*i* are the *i*th wheelset on the windward side and leeward side respectively, *i* = 1, 3).

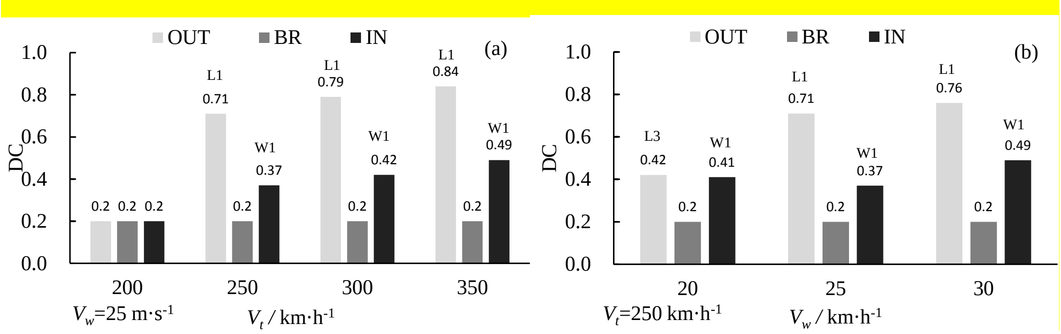

Fig. 22. The maximum peaks of DC in different train and crosswind speeds with wind barriers (W*i* and L*i* are the *i*th wheelset on the windward side and leeward side respectively, *i* = 1,2,3,4).

Declaration of interests

Title: **Aerodynamic response of high-speed trains under crosswind at bridge–tunnel section with or without wind barrier**

The authors declare that they have no known competing financial interests or personal relationships that could have appeared to influence the work reported in this paper.

E Deng

CRediT authorship contribution statement

Weichao Yang: Conceptualization, Investigation, Writing-review & editing. **E Deng**: Methodology, Software, Writing-original draft. **Xuhui He**: Funding acquisition, Validation, Writing-review & editing. **Zhihui Zhu**: Resources, Writing-review & editing. **Ang Wang**: Data curation, Investigation. **Zhao Wen**: Writing-review & editing.